



GEORG-AUGUST-UNIVERSITÄT  
GÖTTINGEN

Fakultät für  
Physik 

## Bachelor's Thesis

# Interpolation von QCD Wirkungsquerschnitten unter Verwendung von APPLGRID und fastNLO

## Interpolation of QCD cross sections using APPLGRID and fastNLO

prepared by

**Timo Janßen**

from Westerstede

at the II. Physikalisches Institut

**Thesis period:** April 23, 2015 until July 30, 2015

**First referee:** Jun.-Prof. Dr. rer. nat. Steffen Schumann

**Second referee:** Prof. Dr. Arnulf Quadt



## Abstract

Timo Janßen

### Interpolation of QCD cross sections using APPLGRID and fastNLO

The interpolation methods implemented by `APPLGRID` and `fastNLO` are validated for inclusive Higgs boson production at the 13 TeV LHC. Different final state jet multiplicities are studied. It is verified that the method accurately reproduces observables with *a posteriori* parameter variation. The `MCgrid` software is used to interface the interpolation tools and automatically produce interpolation grids for fixed order NLO calculations.

**Key words:** perturbative QCD; NLO QCD calculations; Monte Carlo event generator; PDF



---

## Contents

---

<b>1</b>	<b>Introduction</b>	<b>1</b>
<b>2</b>	<b>Theoretical foundations</b>	<b>3</b>
2.1	Basics of perturbative QCD . . . . .	3
2.1.1	Renormalization and the running coupling . . . . .	4
2.2	The Parton Model . . . . .	5
2.2.1	Hadron-Hadron Cross Sections . . . . .	6
2.3	Corrections to the naive parton model . . . . .	6
2.3.1	Factorization . . . . .	8
2.3.2	Evolution . . . . .	8
2.4	Parton shower . . . . .	9
2.5	Next-to-leading order calculations . . . . .	11
2.6	Reweighting QCD calculations . . . . .	13
2.7	Interpolation grids . . . . .	15
2.8	The considered process: Higgs production through gluon fusion . . . . .	17
2.9	Leptonic Higgs decay . . . . .	21
<b>3</b>	<b>Experimentelle Vorgehensweise</b>	<b>23</b>
3.1	??? . . . . .	23
<b>4</b>	<b>Results</b>	<b>27</b>
4.1	Study of the Higgs transverse momentum . . . . .	27
4.2	Grid validation . . . . .	30
4.2.1	Interpolation accuracy . . . . .	30

4.3 Application example: PDF uncertainty in cross section calculations . . .	37
4.4 Application example: Detailed scale dependence of the cross section . . .	38
<b>5 Diskussion</b>	<b>41</b>
<b>6 Conclusion</b>	<b>43</b>
 <b>Appendix</b>	 <b>51</b>
<b>Bibliography</b>	<b>51</b>
<b>Todo list</b>	<b>58</b>





# CHAPTER 1

---

## Introduction

---



# CHAPTER 2

---

## Theoretical foundations

---

### 2.1 Basics of perturbative QCD

QCD is the quantum field theory that describes the strong interactions between Quarks and Gluons. Mathematically, it is a non-abelian gauge theory with symmetry group  $SU(3)$ . Its Lagrangian is given by

$$\mathcal{L}_{\text{QCD}} = \sum_q \bar{\psi}_{q,a} (i\gamma^\mu \partial_\mu \delta_{ab} - g_s \gamma^\mu t_{ab}^C \mathcal{A}_\mu^C - m_q \delta_{ab}) \psi_{q,b} - \frac{1}{4} F_{\mu\nu}^A F^{A\mu\nu}, \quad (2.1)$$

where the sum goes over all quark flavors. The  $\psi_{q,a}$  are quark-field spinors, where  $a = 1 \dots 3$  denotes the color index, and the  $\mathcal{A}_\mu^C$  are gluon fields with a color index  $C = 1 \dots 8$ . The strong coupling constant is denoted by  $g_s$ . Quarks transform under the fundamental representation of  $SU(3)$  while gluons transform under the adjoint representation. The  $t_{ab}^C$  are the generators of the group. The gluon field tensor  $F_{\mu\nu}^A$  is given by

$$F_{\mu\nu}^A = \partial_\mu \mathcal{A}_\nu^A - \partial_\nu \mathcal{A}_\mu^A - g_s f_{ABC} \mathcal{A}_\mu^B \mathcal{A}_\nu^C, \quad (2.2)$$

where the  $f_{ABC}$  are the structure constants of the group, defined through  $[t^A, t^B] = i f_{ABC} t^C$ . In comparison to quantum electrodynamics (QED), the main difference is the presence of the interaction term  $-g_s f_{ABC} \mathcal{A}_\mu^B \mathcal{A}_\nu^C$  which results in the existence of 3-gluon and 4-gluon vertices.

The perturbative approach to QCD is to write the observables as a power series in  $\alpha_s = g_s^2/(4\pi)$ :

$$F = F^{(1)}\alpha_s + F^{(2)}\alpha_s^2 + \dots , \quad (2.3)$$

where  $\alpha_s \ll 1$  so that the series can be truncated after a few terms to obtain a useful approximation. A straightforward way to determine the coefficients is the use of Feynman Diagrams.

### 2.1.1 Renormalization and the running coupling

Calculations in perturbative QCD involve UV-divergent diagrams such as the one illustrated in fig. 2.1, which gives a contribution to the gluon self-energy. Luckily QCD is a renormalizable theory and therefore the divergences can be handled by regularization and renormalization. As a consequence, the quantities appearing in the Lagrangian (the “bare” quantities) are not the same as the quantities we observe physically. The measured values depend on the energy scale, called *renormalization scale*  $\mu_R$ , at which they are evaluated. This scale is arbitrary and unphysical and if we consider the whole perturbative series, the scale dependence vanishes. The scale dependence can be described by differential equations known as *renormalization group equations*. For example, the equation for the coupling constant takes the form

$$\frac{d\alpha_s(\mu_R^2)}{d\ln \mu_R^2} = \beta(\alpha_s(\mu_R^2)) = -\alpha_s^2(b_0 + b_1\alpha_s + b_2\alpha_s^2 + \dots). \quad (2.4)$$

The minus sign in eq. (2.4) is responsible for the asymptotic freedom of QCD: As the momentum transfer becomes large, the strong coupling becomes weak so that quarks and gluons nearly behave as if they were free particles.

In leading order the analytic solution for eq. (2.4) is known as *running coupling* and

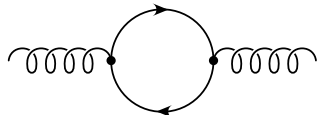


**Figure 2.1:** UV-divergent loop diagram

given by

$$\alpha_s(\mu_R^2) = \frac{\alpha_s(\mu_0^2)}{1 + b_0 \alpha_s(\mu_0^2) \ln \frac{\mu_R^2}{\mu_0^2}} = \frac{1}{b_0 \ln \frac{\mu_R^2}{\Lambda^2}} \quad \text{with} \quad b_0 = \frac{11N_C - 2n_f}{12\pi}, \quad (2.5)$$

where  $N_C$  is the number of colors and  $n_f$  denotes the number of flavors. Note that this is only valid at scales where  $n_f$  does not change. The first expression uses a reference scale  $\mu_0$ , where the value of  $\alpha_s$  is known whereas the second one uses the constant  $\Lambda$ , which is the scale where the coupling would diverge.

## 2.2 The Parton Model

The parton model was introduced in 1969 by Richard P. Feynman to describe high-energy particle collisions involving hadrons [1]. The basic assumption of the parton model is that all hadrons consist of point-like particles (partons) which are responsible for their behavior in interactions. In QCD these can be identified as quarks and gluons. Furthermore, it is assumed that the hadron is in a reference frame where it carries infinite (or at least very high) momentum. In this infinite momentum frame the hadron suffers both Lorentz contraction and time dilation so that the distribution of partons within it does not change during the (vanishingly small) time of interaction. Thus each parton carries a definite fractional momentum  $x$ , with  $0 < x < 1$ . In addition, the process of hadronization due to quark confinement happens too late to influence the interaction. Another important consequence is that the probability of a parton influencing the scattering of another parton is suppressed (“incoherence” of the parton model). The reason this model works is the asymptotic freedom of the underlying theory. However, this also limits the applicability of the parton model to high energy cross sections.

With the help of perturbative QCD, there is a class of reactions involving hadrons for which the cross sections can be calculated directly. These reactions are inclusive and do not contain any hadrons in the initial state. A simple example is lepton pair annihilation into hadrons. As the hadronic final state is fully inclusive, the cross section is identical to the electroweak cross section for  $l + l' \rightarrow q\bar{q}$ , where  $l$  and  $l'$  denote leptons and  $q$  ( $\bar{q}$ ) denotes a (anti-)quark. Assuming  $e^+e^-$  annihilation and

energies much less than the Z boson mass, the total cross section is therefore given by

$$\sigma_{e^+e^- \rightarrow q\bar{q}}(s) = \frac{4\pi\alpha^2}{3s} \cdot 3 \sum_f Q_f^2, \quad (2.6)$$

where the sum is over all quark flavors that can be produced at the center-of-mass energy  $\sqrt{s}$  and the factor 3 is the number of colors [2].

### 2.2.1 Hadron-Hadron Cross Sections

One of the achievements of the parton model is the prediction of cross sections for hadron-hadron collisions such as the *Drell-Yan process*  $h(p) + h'(p') \rightarrow l(k) + l'(k') + X$ . That is possible because PDFs are universal between reactions, so they can be determined once and used to calculate different cross sections. In general, the cross section for a hard scattering process involving two initial hadrons can be written as

$$\sigma(p, p') = \sum_{i,j} \int d\xi d\xi' \phi_{i/h}(\xi) \cdot \sigma_{ij}(\xi p, \xi' p', \alpha_s(\mu^2)) \cdot \phi_{j/h'}(\xi'). \quad (2.7)$$

## 2.3 Corrections to the naive parton model

In order to analyze the effects of higher order corrections, let us reconsider the case of  $e^+e^-$  annihilation into hadrons. The Born cross section is given by eq. (2.6). The first correction towards NLO is the emission of a gluon by one of the quarks (see fig. 2.2). Considering soft emission only, one can show that the differential cross

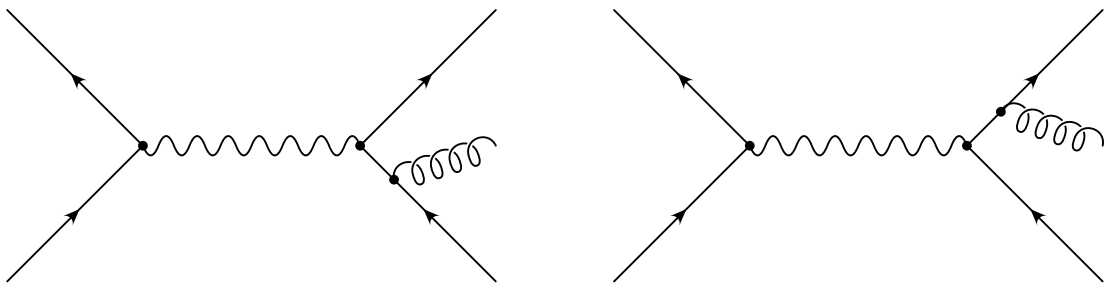


**Figure 2.2:** Feynman diagrams for gluon emission in  $e^+e^-$  annihilation

section for this process factorizes so that one can write

$$|\mathcal{M}_{q\bar{q}g}|^2 d\Phi_{q\bar{q}g} \simeq |\mathcal{M}_{q\bar{q}}|^2 d\Phi_{q\bar{q}} dS . \quad (2.8)$$

The squared matrix element and phase space for  $q\bar{q}$  production plus the emission of a soft gluon is given by the Born squared matrix element and phase space multiplied by a factor  $dS$ , which is the probability for the emission of a soft gluon:

$$dS = \frac{2\alpha_s C_F}{\pi} \frac{dE}{E} \frac{d\theta}{\sin \theta} \frac{d\phi}{2\pi} . \quad (2.9)$$

There are two divergences in this equation: In the limit  $E \rightarrow 0$  there is an infrared divergence and in the limit  $\theta \rightarrow 0, \pi$  there is a collinear divergence when the gluon and quark move in the same direction. These divergences always appear when a gluon is emitted by a quark [3].

Additionally to the real emissions in fig. 2.2 there are virtual emissions shown in fig. 2.3, which we have not taken into account yet. As the total cross section must be finite, the divergences in the real term must be canceled by the virtual term (this can, for example, be shown by the use of dimensional regularization [4]). Therefore the corrections to the total cross section are dominated by hard, large-angle gluons and for these perturbation theory is applicable [3]. Observables that are insensitive to the emission of soft or collinear gluons, like the total cross section for  $e^+e^- \rightarrow \text{hadrons}$ , are called *infrared safe*.

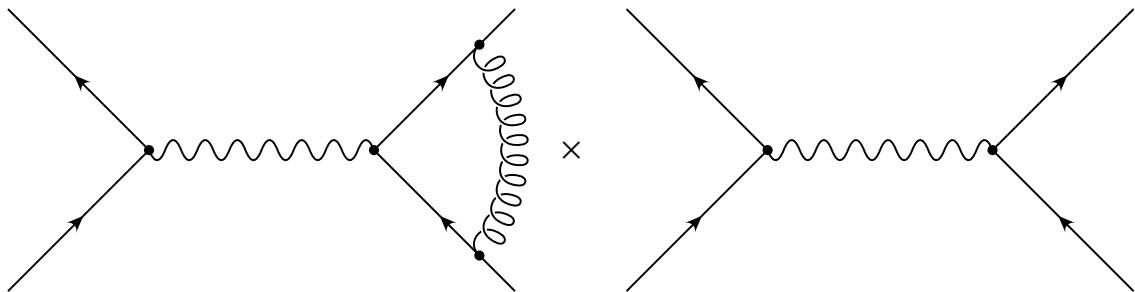


**Figure 2.3:** Virtual correction in  $e^+e^-$  annihilation

### 2.3.1 Factorization

In processes involving initial-state hadrons, the partons can emit gluons before entering the hard interaction (see fig. 2.4). However, there is an important difference between real and virtual emissions in this case: While the virtual emission does not change the momentum of the parton entering the process, the real gluon carries off parts of the parton momentum. Thus, the total cross section consists of two different hard cross sections that do not cancel in the collinear limit. This is a consequence of the collinear limit corresponding to long-range effects of the strong interaction, which are not calculable in perturbation theory.

In order to be able to calculate cross sections with initial-state hadrons, we can take a similar approach as for the renormalization of the coupling constant and introduce a scale variable which we call the *factorization scale*  $\mu_F$ . All the non-perturbative parts are cut off at  $\mu_F$  and absorbed into the PDF. There is an arbitrariness in how much of the correction terms is to be factored out. This is defined by the *factorization scheme*. Common schemes include the DIS scheme, in which all non-leading order contributions are absorbed into the PDFs, and the  $\overline{MS}$  scheme, in which only the divergent parts are absorbed. Once the factorization scheme has been chosen, it has to be used consistently in all following cross section calculations.

### 2.3.2 Evolution

There is an analog for the renormalization group equation for factorization, called the Dokshitzer-Gribov-Lipatov-Altarelli-Parisi (DGLAP) equation. For a quark entering

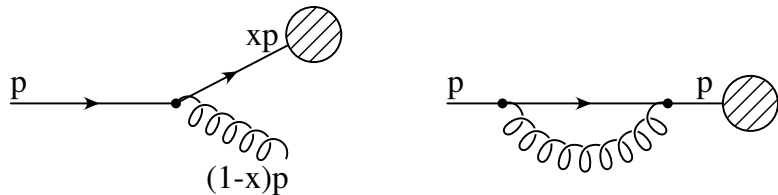


**Figure 2.4:** Feynman diagrams for initial-state gluon emission

the hard process with longitudinal momentum  $xp$  it takes the form

$$\frac{dq(x, \mu_F^2)}{d\ln \mu_F^2} = \frac{\alpha_s}{2\pi} \int_x^1 dz P_{qq}(z) \frac{q(x/z, \mu_F^2)}{z}, \quad (2.10)$$

where  $q(x/z, \mu_F^2)$  is the quark distribution. The function  $P_{qq}(z)$  is called splitting kernel. It has a perturbative expansion in  $\alpha_s$ :

$$P_{qq}(z) = P_{qq}^{(0)}(z) + \frac{\alpha_s}{2\pi} P_{qq}^{(1)}(z) + \dots . \quad (2.11)$$

As the proton does not only contain quarks but also antiquarks and gluons, the actual DGLAP equation is a matrix equation:

$$\frac{d}{d\ln \mu_F^2} \begin{pmatrix} q_i \\ g \end{pmatrix} = \frac{\alpha_s(\mu_F^2)}{2\pi} \begin{pmatrix} P_{q_i q_j} & P_{q_i g} \\ P_{g q_j} & P_{gg} \end{pmatrix} \otimes \begin{pmatrix} q_j \\ g \end{pmatrix}. \quad (2.12)$$

All splitting kernels can be written as perturbative series and have been calculated up to next-to-next-to-leading-order[5, 6]. The DGLAP equation allows to calculate the scale dependence of the PDFs and therefore is an important and powerful tool for PDF fits.

## 2.4 Parton shower

There are phase space regions that cannot be well described by fixed order calculations in perturbation theory. These include collinear parton splitting and soft gluon emission, which are closely related to the presence of infrared divergences. To describe them accurately, higher order terms need to be considered. However, the work required to derive the needed matrix elements quickly increases with each order, which is the reason why most processes have not been calculated further than NLO. We need a different approach to deal with the problematic phase space regions. Instead of relying on a fixed order calculation, we can consider an approximate model that includes the dominant contributions at all orders. In this model, the collinear splitting and soft gluon emission of every parton in the initial and final state is simulated with respect to the related probabilities. The additional partons are again

able to split or radiate gluons. By recursively applying this procedure, we obtain a cascade of parton emissions, called a *parton shower*. An example is illustrated in fig. 2.5. The shower ends when a certain cut-off scale is reached.

The evolution of the splitting with the decreasing scale is given by the DGLAP equation eq. (2.12). In this context the PDFs do not describe the momentum distributions of the partons inside of a hadron, but rather the distribution of the momentum fractions of the partons resulting from the splitting.

The computation of parton showers can be formulated in a way that is well suited for a Monte Carlo program. When the parton shower program is combined with a hadronization model, that combines both the initial state and the final state partons into colorless hadrons, we call the result a *parton shower Monte Carlo event generator*. It is a powerful tool that is able to fully simulate QCD events in hadron collisions.

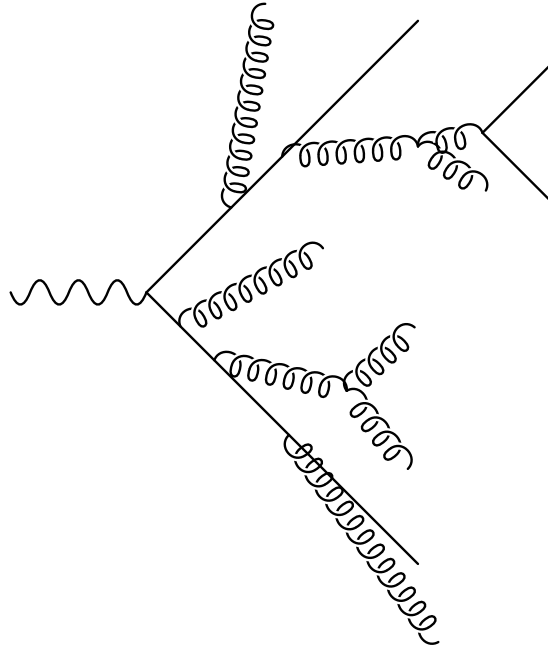


**Figure 2.5:** Example of a parton shower.

## 2.5 Next-to-leading order calculations

... (need real and virtual, both separately divergent, need to regularize)

There are two general methods that are commonly used to take care of the infrared divergences in NLO calculations, namely the *slicing method* and the *subtraction method*. We can demonstrate both methods with a simple example similar to the depiction in [7]. Consider the integral

$$I = \lim_{\epsilon \rightarrow 0} \left( \int_0^1 \frac{dx}{x} x^\epsilon F(x) - \frac{1}{\epsilon} F(0) \right), \quad (2.13)$$

where  $F(x)$  is an arbitrary function that depends on  $x$ . The first term contains a singularity at  $x = 0$  and is divergent in the limit  $\epsilon \rightarrow 0$ . This divergence is canceled by the second term. The parameter  $\epsilon$  can be compared to the parameter used in dimensional regularization. As a consequence of  $F(x)$  being arbitrary complex, the integral can not be solved analytically. However, in this form it is also not well-suited for a numerical evalution because of the presence of  $\epsilon$  in the integrand.

In the slicing method, one introduces a small parameter  $\delta$ , which slices the integration region into two pieces, so that the integral can be written in the following way:

$$\begin{aligned} I &= \lim_{\epsilon \rightarrow 0} \left( \int_0^\delta \frac{dx}{x} x^\epsilon F(x) + \int_\delta^1 \frac{dx}{x} x^\epsilon F(x) - \frac{1}{\epsilon} F(0) \right) \\ &= \lim_{\epsilon \rightarrow 0} \left( F(0) \int_0^\delta \frac{dx}{x} x^\epsilon - \frac{1}{\epsilon} F(0) \right) + \int_\delta^1 \frac{dx}{x} F(x) + \mathcal{O}(\delta) \\ &= F(0) \lim_{\epsilon \rightarrow 0} \frac{\delta^\epsilon - 1}{\epsilon} + \int_\delta^1 \frac{dx}{x} F(x) + \mathcal{O}(\delta) \\ &= F(0) \ln \delta + \int_\delta^1 \frac{dx}{x} F(x) + \mathcal{O}(\delta). \end{aligned} \quad (2.14)$$

Therefore, the dependence on  $\epsilon$  has vanished completely and the remaining integral can be computed numerically. The terms  $\mathcal{O}(\delta)$  are neglectable if  $\delta$  is small. In an actual calculation, one would have to check that the result does not depend on the

choice of  $\delta$ .

The subtraction method does not involve any approximations. Instead, one rewrites the integral in the form

$$\begin{aligned} I &= \lim_{\epsilon \rightarrow 0} \left( \int_0^1 \frac{dx}{x} x^\epsilon [F(x) - F(0)] + F(0) \int_0^1 \frac{dx}{x} x^\epsilon - \frac{1}{\epsilon} F(0) \right) \\ &= \int_0^1 \frac{dx}{x} [F(x) - F(0)], \end{aligned} \quad (2.15)$$

which automatically leads to a form that can be evaluated by a numerical integration algorithm. We can take a look at how this method works in a somewhat more realistic calculation. Consider the expression for the expectation value of an infrared-safe observable  $O$  at NLO accuracy, consisting of a Born (B), a virtual (V) und a real (R) term:

$$\langle O \rangle = \lim_{\epsilon \rightarrow 0} \int_0^1 dx x^{-2\epsilon} O(x) \left[ \left( \frac{d\sigma}{dx} \right)_B + \left( \frac{d\sigma}{dx} \right)_V + \left( \frac{d\sigma}{dx} \right)_R \right]. \quad (2.16)$$

We assume that the cross sections can be written as

$$\left( \frac{d\sigma}{dx} \right)_B = B \delta(x), \quad (2.17)$$

$$\left( \frac{d\sigma}{dx} \right)_V = a \left( \frac{B}{2\epsilon} + V \right) \delta(x), \quad (2.18)$$

$$\left( \frac{d\sigma}{dx} \right)_R = a \frac{R(x)}{x} \quad (2.19)$$

where  $B$  and  $V$  are constant factors and  $\lim_{x \rightarrow 0} R(x) = B$ .  $a$  denotes the coupling constant. This model has been adapted from [8]. Obviously, both the real and the virtual part are divergent in the limit  $\epsilon \rightarrow 0$ . Using the subtraction method

analogous to the case above, we can rewrite the real contribution to obtain

$$\begin{aligned}\langle O \rangle_R &= a \lim_{\epsilon \rightarrow 0} \int_0^1 \frac{dx}{x^{1+2\epsilon}} O(x) R(x) \\ &= a BO(0) \lim_{\epsilon \rightarrow 0} \int_0^1 \frac{dx}{x^{1+2\epsilon}} + a \int_0^1 \frac{dx}{x} [O(x) R(x) - BO(0)] \\ &= -a BO(0) \lim_{\epsilon \rightarrow 0} \frac{1}{2\epsilon} + a \int_0^1 \frac{dx}{x} [O(x) R(x) - BO(0)].\end{aligned}\quad (2.20)$$

By explicitly writing down the virtual part,

$$\langle o \rangle_V = a \lim_{\epsilon \rightarrow 0} \int_0^1 \frac{dx}{x^{2\epsilon}} O(x) \left( \frac{B}{2\epsilon} + V \right) \delta(x), \quad (2.21)$$

we see that the first term gets exactly cancelled by the first term on the right hand side of (2.20). Including the Born contribution we arrive at the expression

$$\langle O \rangle = BO(0) + a \left\{ VO(0) + \int_0^1 \frac{dx}{x} [O(x) R(x) - BO(0)] \right\}, \quad (2.22)$$

which now only consists of finite terms.

The subtraction method can be generalized to arbitrary hadronic cross sections, provided that the definition of the observables allows the cancellation of the divergences. In simplified terms, it always leads to an expression of the form

$$\sigma_{pp \rightarrow X}^{\text{NLO}} = \int d\hat{\sigma}^B + \int d\hat{\sigma}^V + \int d\hat{\sigma}^I + \int d\hat{\sigma}^{RS} \quad (2.23)$$

consisting of a Born (B), a virtual (V), an integrated subtraction (I) and a real subtracted (RS) term. All of these terms are separately finite.

## 2.6 Reweighting QCD calculations

Often it is needed to vary the parameters in QCD calculations, for example the scale variables and PDFs to estimate the uncertainty. When the number of variations becomes large, it is not practical to rerun the whole event generation for each

calculation as the time and resource consumption become too high. Instead it is possible to reuse information from previously generated events and combine them with the new parameters. For a leading order calculation, this is straightforward: Consider the leading order parton model cross section for producing an arbitrary final state  $X$ :

$$\sigma_{pp \rightarrow X} = \sum_{i,j} \int dx_1 dx_2 \int d\Phi_n \left( \frac{\alpha_s(\mu_R^2)}{2\pi} \right)^{p_{\text{LO}}} f_i(x_1, \mu_F^2) f_j(x_2, \mu_F^2) d\hat{\sigma}_{ij \rightarrow X}. \quad (2.24)$$

The squared matrix element for the parton-level subprocess  $2 \rightarrow n$  is denoted by  $d\hat{\sigma}_{ij \rightarrow X}$ , differential in the phase space  $d\Phi_n$ . We can group subprocesses  $s$  with the same parton-level cross section into a cumulated parton density  $F_s(x_1, x_2, \mu_F^2)$  and write

$$\sigma_{pp \rightarrow X} = \int dx_1 dx_2 \int d\Phi_n \left( \frac{\alpha_s(\mu_R^2)}{2\pi} \right)^{p_{\text{LO}}} F_s(x_1, x_2, \mu_F^2) d\hat{\sigma}_{ij \rightarrow X}. \quad (2.25)$$

Rewriting this in a form that can be computed by a Monte Carlo algorithm on a per-event basis, we arrive at

$$\sigma_{pp \rightarrow X} = \sum_{e=1}^{N_{\text{evt}}} \left( \frac{\alpha_s(\mu_R^2)}{2\pi} \right)^{p_{\text{LO}}} w_e(k_e) F_{s_e}(x_1, x_2, \mu_F^2). \quad (2.26)$$

The event weight  $w_e(k_e)$  is given by

$$w_e(k_e) = \Pi_{\text{ps}}(k_e) \Theta(k_e - k_{\text{cuts}}) d\hat{\sigma}_e \quad (2.27)$$

and represents the subprocess cross section  $d\hat{\sigma}_e$  with respect to the phase space weight  $\Pi_{\text{ps}}(k_e)$  and the kinematic cuts. The kinematic parameters for each event are combined in

$$k_e = \{p_1, \dots, p_n, x_1, x_2\}, \quad (2.28)$$

where the  $p_i$  denote the involved partons.

Provided that all event weights have been stored, using a different PDF is as simple as multiplying each weight with the new PDF  $F_{s_e}^{\text{new}}(x_1, x_2, \mu_F^2)$ . The value of  $\alpha_s$  can be changed similarly. To vary the scales, only  $\alpha_s$  and  $F_{s_e}$  have to be reevaluated as the weights themselves do not depend on the scales.

At NLO the reweighting becomes more involved. The event weights now depend explicitly on the scales and due to the appearance of divergences in the calculation of the parton-level cross sections, a method for cancelling these divergences has to be used. In the following, we will examine the method used by **MCgrid** to reweight NLO calculations. It expects, that the events are generated using the Catani-Seymour dipole subtraction method [9], which is a general algorithm for the automatic calculation of arbitrary jet cross sections at NLO. It is based on the subtraction method introduced in §2.5.

As we have seen, the subtraction method splits the calculation into four parts: The Born (B), virtual (V), integrated subtraction (I) and real subtraction (RS) part. All of these have to be handled differently. How this is done in detail can be seen in the original **MCgrid** paper [10]. The important result is, that if we treat the different contributions as single events, the NLO result can be written in a form similar to the LO expression (2.26):

$$\sigma_{pp \rightarrow X}^{\text{NLO}} = \sum_{e=1}^{N_{\text{evt}}} \left( \frac{\alpha_s(\mu_R^2)}{2\pi} \right)^{p_e} w_e(k_e) F_{s_e}(x_1, x_2, \mu_F^2), \quad (2.29)$$

where  $p_e$  is the order in  $\alpha_s$  of the respective event, i.e.  $p_e = p_{\text{LO}}$  for B events and  $p_e = p_{\text{LO}} + 1$  for I, V and RS events. This allows for simple *a posteriori* parameter variation analogous to the LO case.

## 2.7 Interpolation grids

Despite the advantage towards regenerating all events for the variation of a single parameter, the reweighting approach is still not a satisfying solution for many use cases. The whole event record has to be stored, which can easily reach many gigabytes in high statistics computations. The storing and reprocessing of the events may be

a challenge by itself and is not convenient if more than a few parameter variations have to be performed. One therefore wishes to somehow decrease the resource requirements without losing a significant amount of accuracy. In the ideal case, it should be mostly independent on the statistics. A possible solution is the use of interpolating grids to represent the PDFs and event weights. Then only a uniquely defined number of values has to be saved, while values in-between the grid points are generated by interpolating functions. Such a method has been implemented by the **APPLGRID** [11] and **fastNLO** [12, 13] projects.

The PDF  $f(x, Q^2)$  depends on the momentum fraction  $x$  and the momentum transfer  $Q^2$ . It can be approximated as a sum over discrete grid points using interpolation functions  $I$  of order  $N$ :

$$f(x, Q^2) = \sum_{i=0}^{N_x} \sum_{j=0}^{N_Q} f(x_i, Q_j^2) I_i^{(N_x)}(x_1) I_j^{(N_Q)}(Q^2). \quad (2.30)$$

Transferred to the subprocess PDF  $F_s(x_1, x_2, Q^2)$  defined above, the interpolation takes the form

$$F_s(x_1, x_2, Q^2) = \sum_{i,j=0}^{N_x} \sum_{k=0}^{N_Q} F_s(x_i, x_j, Q_k^2) I_i^{(N_x)}(x_1) I_j^{(N_x)}(x_2) I_k^{(N_Q)}(Q^2). \quad (2.31)$$

Consequently, we can write (2.29) as

$$\begin{aligned} \sigma_{pp \rightarrow X}^{\text{NLO}} &= \sum_{e=1}^{N_{\text{evt}}} \sum_{i,j=0}^{N_x} \sum_{k=0}^{N_Q} \left( \frac{\alpha_s(Q_k^2)}{2\pi} \right)^{p_e} w_e(k_e) F_{s_e}(x_i, x_j, Q_k^2) \\ &\quad \cdot I_i^{(N_x)}(x_1) I_j^{(N_x)}(x_2) I_k^{(N_Q)}(Q^2) \\ &= \sum_p \sum_{s=0}^{N_{\text{sub}}} \sum_{i,j=0}^{N_x} \sum_{k=0}^{N_Q} \left( \frac{\alpha_s(Q_k^2)}{2\pi} \right)^p W_{i,j,k}^{(p),(s)}(k_e) F_s(x_i, x_j, Q_k^2), \end{aligned} \quad (2.32)$$

where  $p$  is the perturbative order,  $N_{\text{sub}}$  is the number of different subprocesses and

the interpolated weights  $W_{i,j,k}^{(p),(s)}(k_e)$  are processed as a sum over the events:

$$W_{i,j,k}^{(p),(s)} = \sum_{e=1}^{N_{\text{evt}}} \delta_{p,p_e} \delta_{s,s_e} I_{i,j,k}^{(N_x)(N_Q)}(k_e) w_e(k_e) I_i^{(N_x)}(x_1) I_j^{(N_x)}(x_2) I_k^{(N_Q)}(Q^2). \quad (2.33)$$

Now the sum over the events is completely absorbed into the definition of the interpolated weights. These can be calculated in a single run of the event generator and be stored efficiently. The calculation of the cross section has become a simple sum over the grid points and thus is much faster for a large number of events. The approach can easily be extended to histogrammed data like differential cross sections by defining the observable bins and computing one weight  $W_{i,j,k}^{(p),(s),(b)}$  for each bin  $b$ . However, unlike the full event record, the weight grid is restricted to the observable it was constructed for and cannot be used to calculate any other values.

While the variation of the PDF and  $\alpha_s$  is still straightforward, scale variation is slightly more complicated because the weights themselves depend on the scale choices. Nevertheless, it is possible to vary the scales without too much effort, using DGLAP evolution. The precise procedure is explained in [11].

## 2.8 The considered process: Higgs production through gluon fusion

The Englert-Brout-Higgs-Guralnik-Hagen-Kibble mechanism (commonly Higgs mechanism) explains the non-zero masses of the gauge bosons in the standard model. It has been developed in the 1960s with important contributions coming from several people [14–19]. It invokes the process of spontaneous symmetry breaking and evades the Goldstone theorem. In the development of the standard model, the Higgs mechanism played a key role and ever since its discovery in 2012 by ATLAS [20] and CMS [21] at the LHC it has received wide approval.

In this thesis, the considered process will be the production of a Higgs boson through gluon fusion. Although there are other possible production mechanisms in the Standard Model, this is the main process at the LHC, with an expected cross section of  $\approx 50 \text{ pb}$  at a center-of-mass energy of  $\sqrt{s} = 14 \text{ TeV}$  and a Higgs mass of  $125 \text{ GeV}$  [22]. It proceeds through a triangular loop of heavy quarks (mainly top quarks as the Higgs coupling scales with the quark mass) as is shown in Figure 2.6.

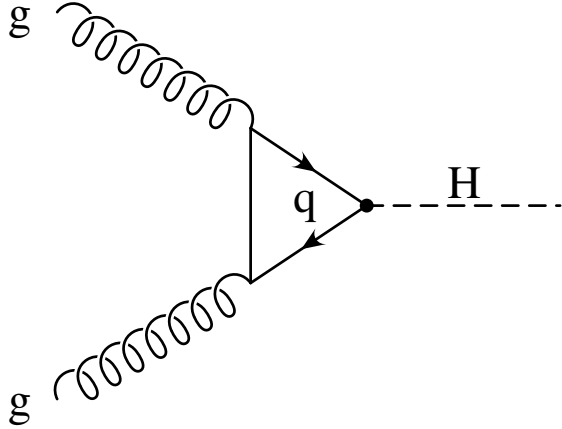


**Figure 2.6:** Higgs production through gluon fusion.

In the narrow-width approximation, the leading order cross section is given by [23]

$$\sigma_{\text{LO}}(pp \rightarrow H) = \sigma_0^H \tau_H \frac{d\mathcal{L}^{gg}}{d\tau_H}, \quad (2.34)$$

where  $\tau_H = M_H^2/s$  is the Drell-Yan variable and  $d\mathcal{L}^{gg}/d\tau_H$  is the gluon luminosity. The partonic cross section  $\sigma_0^H$  can be written as

$$\sigma_0^H = \frac{G_F \alpha_s^2(\mu_R^2)}{288\sqrt{2}\pi} \left| \sum_q \frac{3}{2\tau_q} \left[ 1 + \left( 1 - \frac{1}{\tau_q} \right) f(\tau_q) \right] \right|^2, \quad (2.35)$$

with the form factor

$$f(\tau_q) = \begin{cases} \arcsin^2(\sqrt{\tau_q}), & \tau_q < 1, \\ -\frac{1}{4} \left[ \ln \frac{1+\sqrt{1-\tau_q^{-1}}}{1-\sqrt{1-\tau_q^{-1}}} - i\pi \right]^2, & \tau_q > 1, \end{cases} \quad (2.36)$$

where  $G_F$  denotes the Fermi coupling constant and  $\tau_q = m_H^2/4m_q^2$ . The gluon

luminosity takes the form

$$\frac{d\mathcal{L}^{gg}}{d\tau_H} = \int_0^1 dx_1 dx_2 g(x_1, \mu_F^2) g(x_2, \mu_F^2) \delta(x_1 x_2 - \tau_q) \quad (2.37)$$

with  $g(x, \mu_F^2)$  denoting the gluon PDF.

The QCD corrections are composed of virtual corrections to the vertices and propagators, real gluon radiation in the initial state and the contributions of the subprocesses  $gq \rightarrow Hq$  and  $q\bar{q} \rightarrow Hg$ . Exemplary diagrams for the corrections are shown in Figure 2.7.

The NLO QCD corrections to the cross section have been calculated in [24]. They increase the cross section by a factor of 1.5 to 1.7. In the limit where the top quark has infinite mass,  $m_t \rightarrow \infty$ , the form factor takes the value  $\frac{4}{3}$ . This allows for an analytical expression for the corrections [25], which is very well suited for numerical calculations. It can be considered as an extension of the Standard Model, where the Higgs boson couples directly to gluons (effective Higgs coupling). In many cases, this is a rather good approximation [26].

The NNLO corrections have been calculated in [27, 28].

A fully differential NNLO calculation exists for  $H + 0 - \text{jet}$  production [29, 30] and substantial progress has been achieved towards an NNLO calculation of the  $1 - \text{jet}$  cross section [31]. The fully differential NLO cross section is available for  $H + 1 - \text{jet}$  [32, 33],  $H + 2 - \text{jets}$  [34, 35] and  $H + 3 - \text{jets}$  [36].

The effective Lagrangian for Higgs gluon interaction can be written as [28]

$$\mathcal{L}_{\text{eff}}^{ggH} = -\frac{1}{4v} C_1 G_{\mu\nu}^a G^{a\mu\nu} H, \quad (2.38)$$

where  $v$  is the Higgs vacuum expectation value,  $G_{\mu\nu}^a$  is the gluon field strength tensor

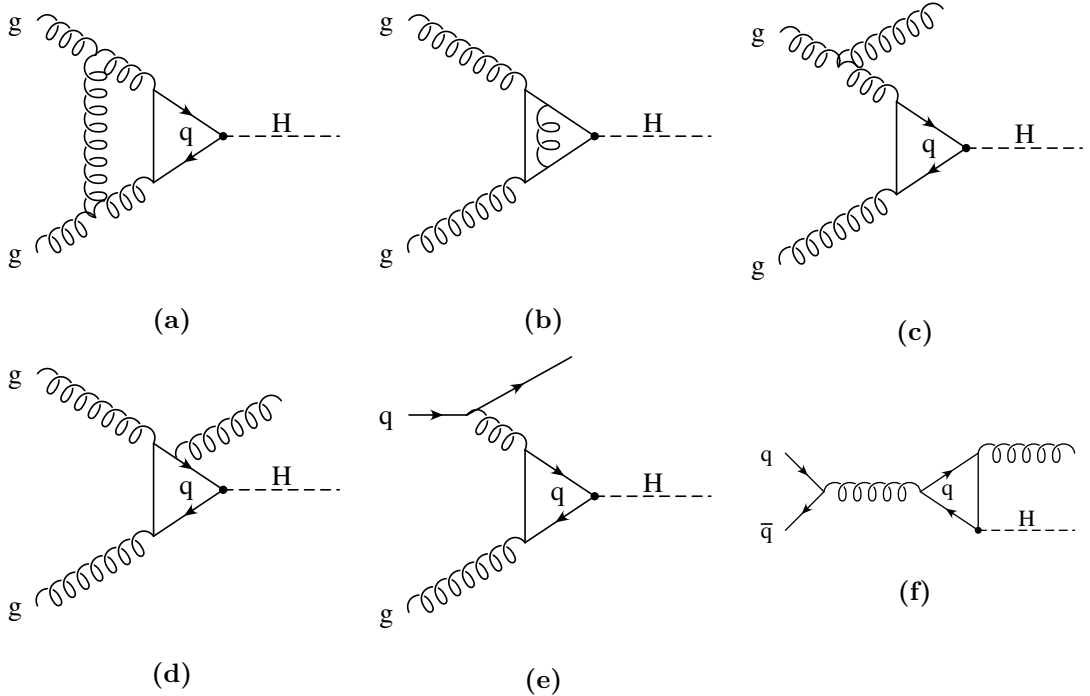


**Figure 2.7:** Example diagrams illustrating the QCD corrections to the process  $pp \rightarrow H$ : (a), (b) virtual corrections; (c), (d) real emission of a gluon; (e)  $gq \rightarrow Hq$ ; (f)  $q\bar{q} \rightarrow Hg$ .

and  $H$  is the Higgs field. The coefficient  $C_1$ , in the  $\overline{\text{MS}}$  scheme, is given by

$$C_1 = \frac{-1}{3\pi} \left\{ 1 + \frac{11\alpha_s}{4\pi} + \left( \frac{\alpha_s}{\pi} \right)^2 \left[ \frac{2777}{288} + \frac{19}{16} \log \left( \frac{\mu^2}{m_t^2} \right) + n_f \left( -\frac{67}{96} + \frac{1}{3} \log \left( \frac{\mu^2}{m_t^2} \right) \right) \right] + \mathcal{O}(\alpha_s^3) \right\}, \quad (2.39)$$

where the number of active flavors should be set to  $n_f = 5$ . According to [28], at LO this approximation is accurate within 5 % for  $m_H \approx 150$  GeV (which is close to the measured value  $m_H \approx 126$  GeV) and improves at NLO.

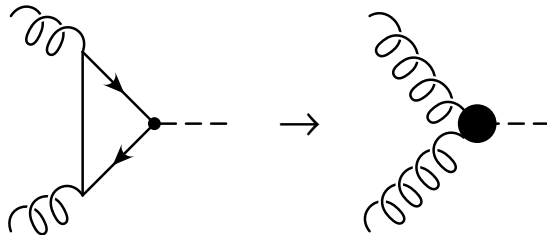


**Figure 2.8:** Effective Higgs coupling.

## 2.9 Leptonic Higgs decay

In an experiment, one would never observe the Higgs boson directly but rather reconstruct it from the measured properties of its decay products. We want to approximate this situation by simulating the Higgs boson decay. There are several possible decay channels. One has to keep in mind that the Higgs coupling is proportional to the particle masses, so that it will decay into the heaviest possible particles. Assuming a Higgs mass of  $m_H = 126 \text{ GeV}$ , the most relevant decay products are  $q\bar{q}$  (where  $q$  denotes a bottom or charm quark),  $WW$ ,  $ZZ$ ,  $Z\gamma$ ,  $\gamma\gamma$ ,  $gg$  and  $\tau^+\tau^-$  [37]. The decay into photons or gluons is only possible through intermediate loops. The studies leading to the discovery of the Higgs boson at the LHC relied primarily on the decay modes  $H \rightarrow \gamma\gamma$ ,  $H \rightarrow ZZ$  and  $H \rightarrow WW$ .

For the purpose of this thesis, we will consider the decay  $H \rightarrow \tau^+\tau^-$ , which has a branching ratio of approximately 6 % [38]. The Feynman diagram is shown in fig. 2.9. It would be possible to simulate the other decay channels as well, however, this would only complicate the analysis unnecessarily. The leptonic decay is the easiest one and closely resembles the Drell-Yan process. There have been searches for  $H \rightarrow \tau\tau$  events in the LHC data and both ATLAS [39] and CMS [40] have published evidence for this type of decay. It also allows for the observation of additional jets that are produced in the initial state and are separated from the Higgs decay products. We will not consider the further decay of the tau leptons, which would naturally occur in the experiment.

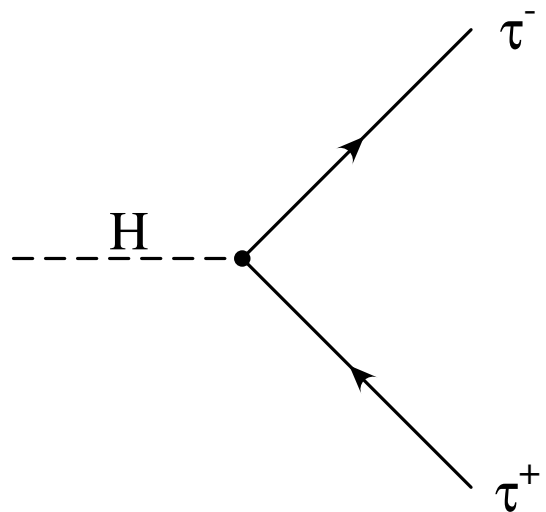


**Figure 2.9:** Higgs decay into two  $\tau$  leptons.

# CHAPTER 3

---

## Experimentelle Vorgehensweise

---

### 3.1 ???

APPLGRID and `fastNLO` do not use the momentum fraction  $x$  and the factorization scale  $Q^2$  directly in their grids. Instead they provide transformations that are supposed to achieve better coverage of the values. In the following we will concentrate on the  $x$  distribution, which is more crucial to the number of grid points needed. The functions provided by APPLGRID are:

$$f_0(x) = \log\left(\frac{1}{x} - 1\right) \quad (3.1)$$

$$f_1(x) = -\log(x) \quad (3.2)$$

$$f_2(x) = \sqrt{-\log(x)} \quad (3.3)$$

$$f_3(x) = -\log(x) + 5 \cdot (1 - x). \quad (3.4)$$

`fastNLO` only provides the functions  $f_1(x)$  and  $f_2(x)$ . To be used in a grid, the functions are divided into equal-sized bins. In order to avoid empty bins, the limit values are determined in a separate “phasespace run” before the actual fill run.

The functions (normalized to the domain  $[0, 1]$  for comparability) are shown in Figure 3.1. All transformations increase the point density in the low  $x$  region, where most events should fall into. Compared against  $f_0$ , the other functions also accomplish a higher point density in the high  $x$  region. Some observables in specific processes might benefit from this.

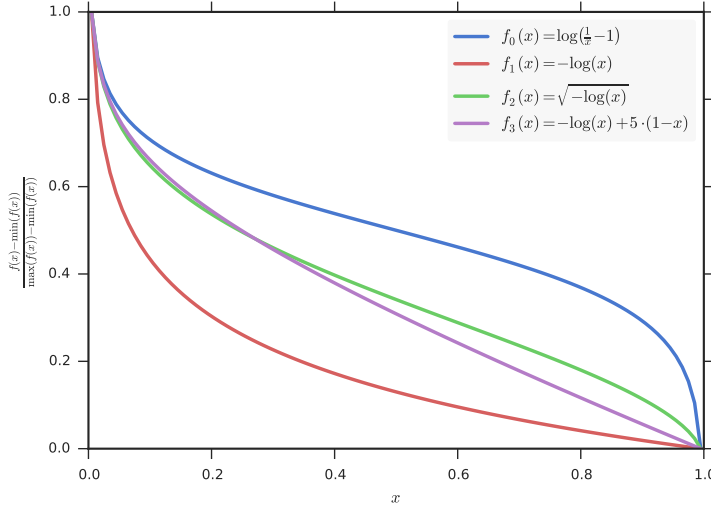


**Figure 3.1:** The transformations applied to the  $x$  distribution, normalized to the range  $[0, 1]$ .

We can look at the actual  $x$  distribution in the process considered in this thesis. In Figure 3.2 it is plotted for one of the gluons involved in the process  $gg \rightarrow H + j$  at leading order for a center-of-mass energy of  $\sqrt{s} = 13$  TeV. For comparison, the respective distribution for the functions  $f_1$  to  $f_4$  is also shown. In the bare distribution, the number of events per bin increases rapidly towards low  $x$ . It is obvious that the reproduction of the low  $x$  region is poor for this linear binning. We expect that for some  $x > 0$  the number of events approaches zero, because there has to be at least enough momentum transfer to produce the Higgs boson and the jet. To see this with linear binning, one would need a huge amount of bins. In contrast, the transformations are able to project the low  $x$  peak to a higher number of bins than the naive linear binning. Additionally, they all approach zero for a finite value (note that high values of  $f(x)$  correspond to low values of  $x$ ). Due to the normalization, this happens at 1. For all transformed distributions, it should be possible to interpolate them with a reasonable number of sampling points. The function  $f_1(x)$  looks most promising, as it allocates many bins for the peak region, which should be the most relevant for this process.

If we want to be more specific, we can extract the dependence of the observables

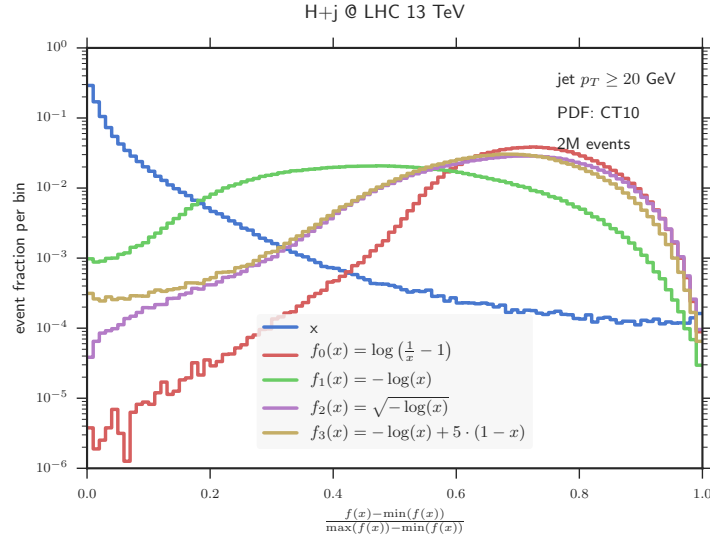


**Figure 3.2:** The event fraction per bin for the different transformations.

on  $x$  and  $f(x)$ , respectively, from the generated events. This is shown in Figure 3.3 for the transverse momentum  $p_\perp$  and in Figure 3.4 for the rapidity  $y$  of the Higgs boson. For both observables all considered functions are reasonable. Again, the function  $f_1(x)$  seems to be best suited. Hence, it will be the transformation used in all following grid calculations.

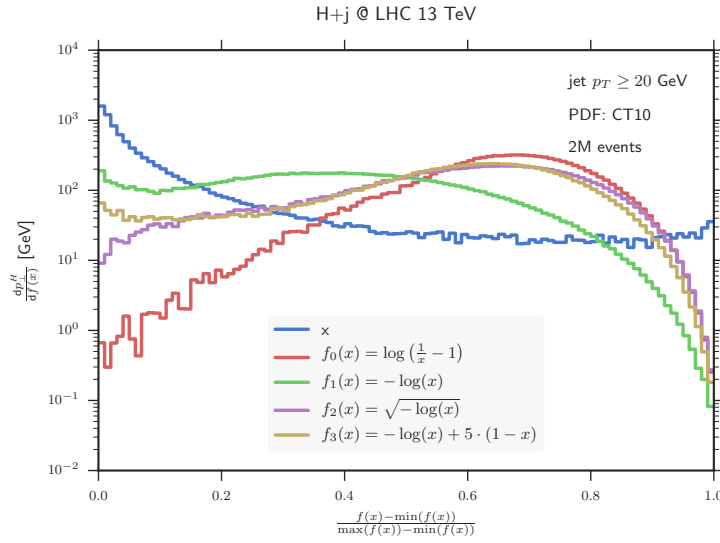


**Figure 3.3:** The transverse momentum  $p_T$  of the Higgs boson differential in the momentum fraction  $x$  of one of the gluons.

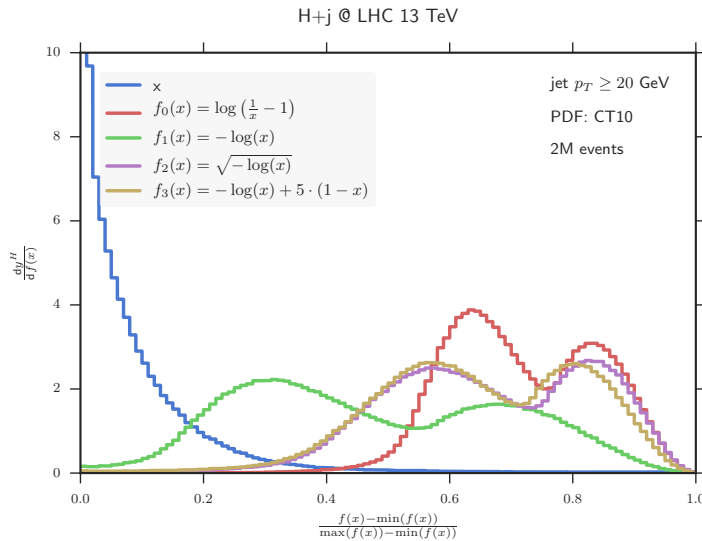


**Figure 3.4:** The rapidity  $y$  of the Higgs boson differential in the momentum fraction  $x$  of one of the gluons.

# CHAPTER 4

---

## Results

---

### 4.1 Study of the Higgs transverse momentum

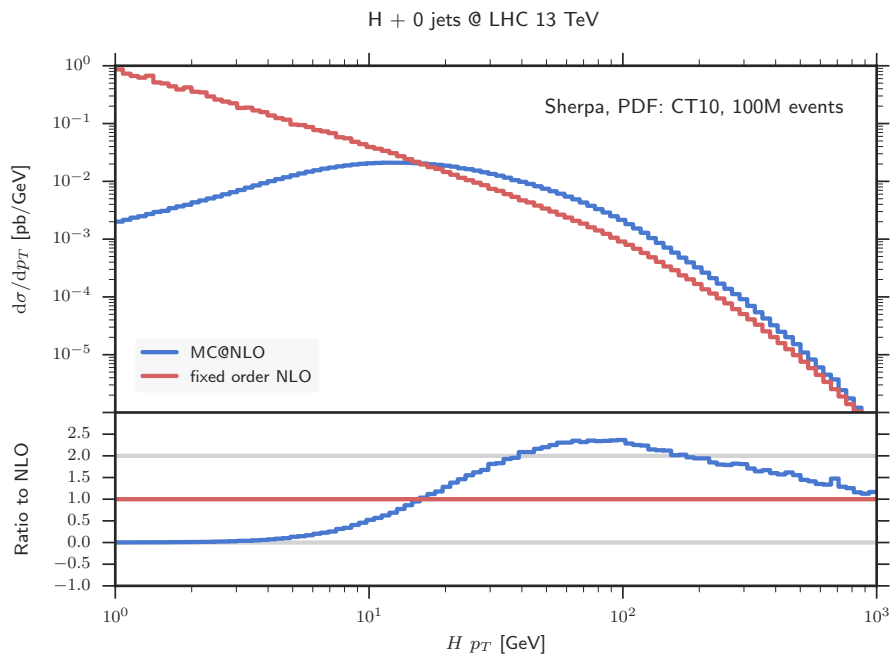
...

Four separate runs have been performed: One run each for zero, one and two jets at fixed order NLO and one **MC@NLO** run merging up to two jets in the core process. The **Rivet** analysis system has been used to extract the transverse momentum of the Higgs boson from the events. In the multijet merged run, the cases of at least zero, one or two jets have been distinguished and sorted into different histograms. Thus, we obtain inclusive observables that are comparable to the fixed order results. **SHERPA** has been used for all calculations and the **MCFM** library [41] has been interfaced for the 2-jet process. For the fixed order calculations, both the renormalization and the factorization scale have been set to the transverse mass of the Higgs boson. Final state jets have been extracted by the **FastJet** library [42] using the anti- $k_t$  algorithm [43] with a radius parameter  $R = 0.4$  and a  $p_{\perp}$ -cut of  $p_{\perp} > 20 \text{ GeV}$ .

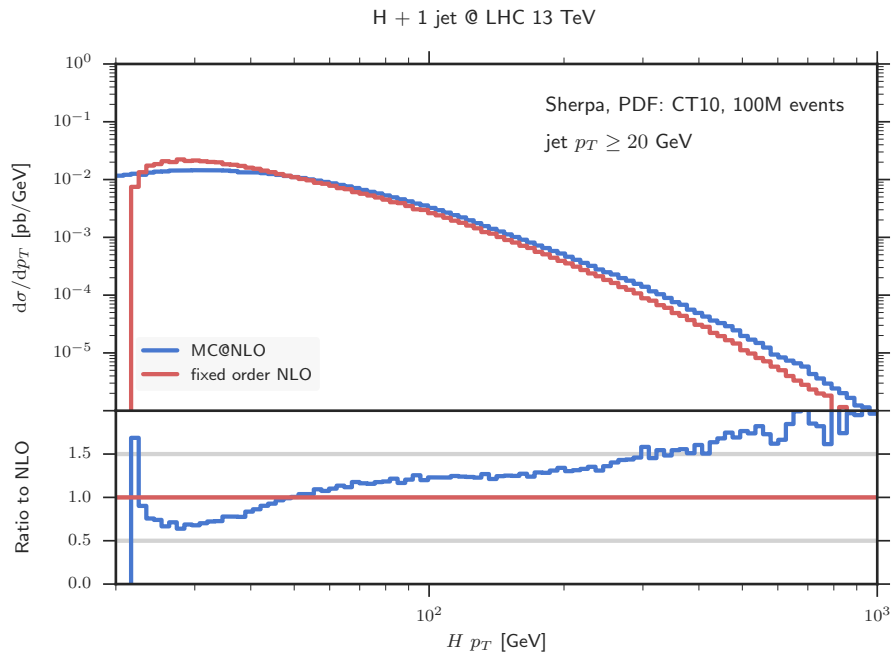
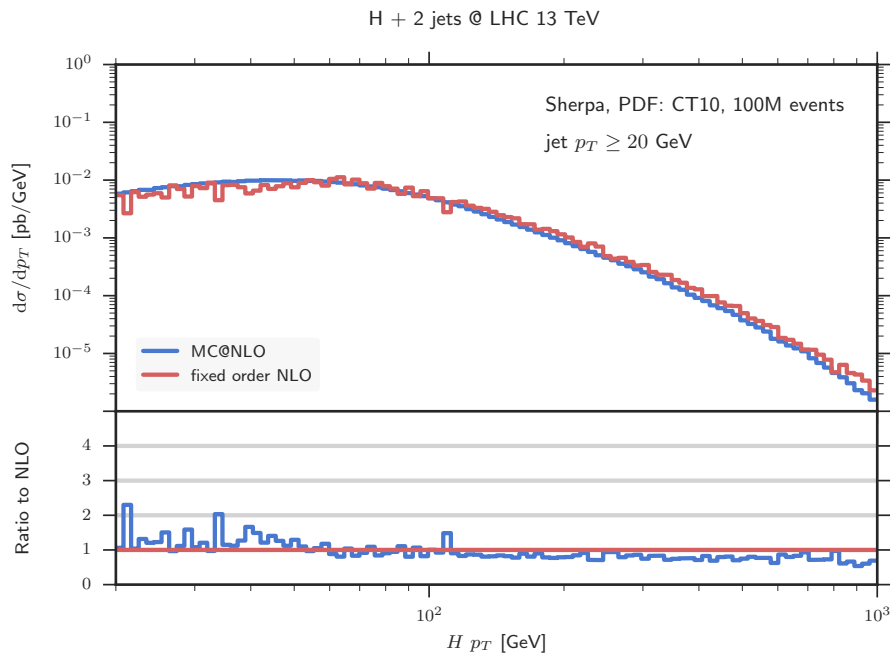
Figure 4.1 compares the fixed order NLO and the merged **MC@NLO** results in the case of no jets. At NLO the transverse momentum of the Higgs boson arises solely from real gluon emissions as the LO process does not have any transverse parts. The splitting leading to the real emissions is divergent in the soft and collinear limits which correspond to low transverse momenta. Therefore, in fig. 4.1, we see that the cross section diverges towards low  $p_{\perp}$ . The multijet result behaves completely different in the low  $p_{\perp}$  region and shows no divergence. In this case, the cross section

is dominated by parton showers which include higher orders and are not divergent. Compared to the fixed order calculation, the cross section is much smaller in the low  $p_{\perp}$  region. As opposed to this, the cross section is amplified for  $p_{\perp} \gtrsim 20$  GeV. The influence of the parton shower is negligible in this region. Instead the additional contributions come from the higher jet multiplicities that have been merged into the calculation. At high  $p_{\perp}$ , both results approach each other.

The results containing one or more jets are compared in fig. 4.2. The total cross section expectably is smaller than in the 0-jet case. Due to the jet cut, the minimum  $p_{\perp}$  of the Higgs boson is 20 GeV. At  $p_{\perp} = 20$  GeV, when the Higgs boson recoils against the jet, the cross section diverges at NLO. Similar to the previous situation, the parton shower fixes the divergence and produces a smooth distribution. At high  $p_{\perp}$  the merged run gives a higher cross section, this time the additional contributions stem from the 2-jet process.



**Figure 4.1:** H pT 0j

**Figure 4.2:** H pT 1j**Figure 4.3:** H pT 2j

## 4.2 Grid validation

In the following we will validate the interpolation method used by `MCgrid` for the processes  $pp \rightarrow H + (0, 1, 2)\text{jets}$  at the 13 TeV LHC, computed at NLO. Thereto, we generate reference distributions for different observables using the `SHERPA` event generator and compare them to the distributions obtained by convoluting a grid with the respective PDF. Additionally, the results from `APPLGRID` and `fastNLO` are compared to each other. All grids are filled using the central value of the CT10 pdf set [44]. The examined observables are the transverse momenta  $p_\perp$  of the Higgs boson and the  $\tau$  leptons, respectively, the rapidity  $y$  of the Higgs boson and the pseudorapidity  $\eta$  of the  $\tau$  leptons. The projection of the observables into histogram bins is accomplished by the `Rivet` analysis system. Final state jets are extracted by the `FastJet` library [42] using the anti- $k_t$  algorithm [43] with a radius parameter  $R = 0.4$  and a  $p_\perp$ -cut of  $p_\perp > 20\text{ GeV}$ .

The first validity test will check whether the grids are able to reproduce the distributions when they are filled with the same events as the reference histograms, i.e. when no parameter variation is performed. This will also determine the interpolation accuracy. Subsequently, the cases where the scale factors and/or PDFs of the grids are changed *a posteriori* will be compared to reference distributions where these parameters have been set explicitly.

### 4.2.1 Interpolation accuracy

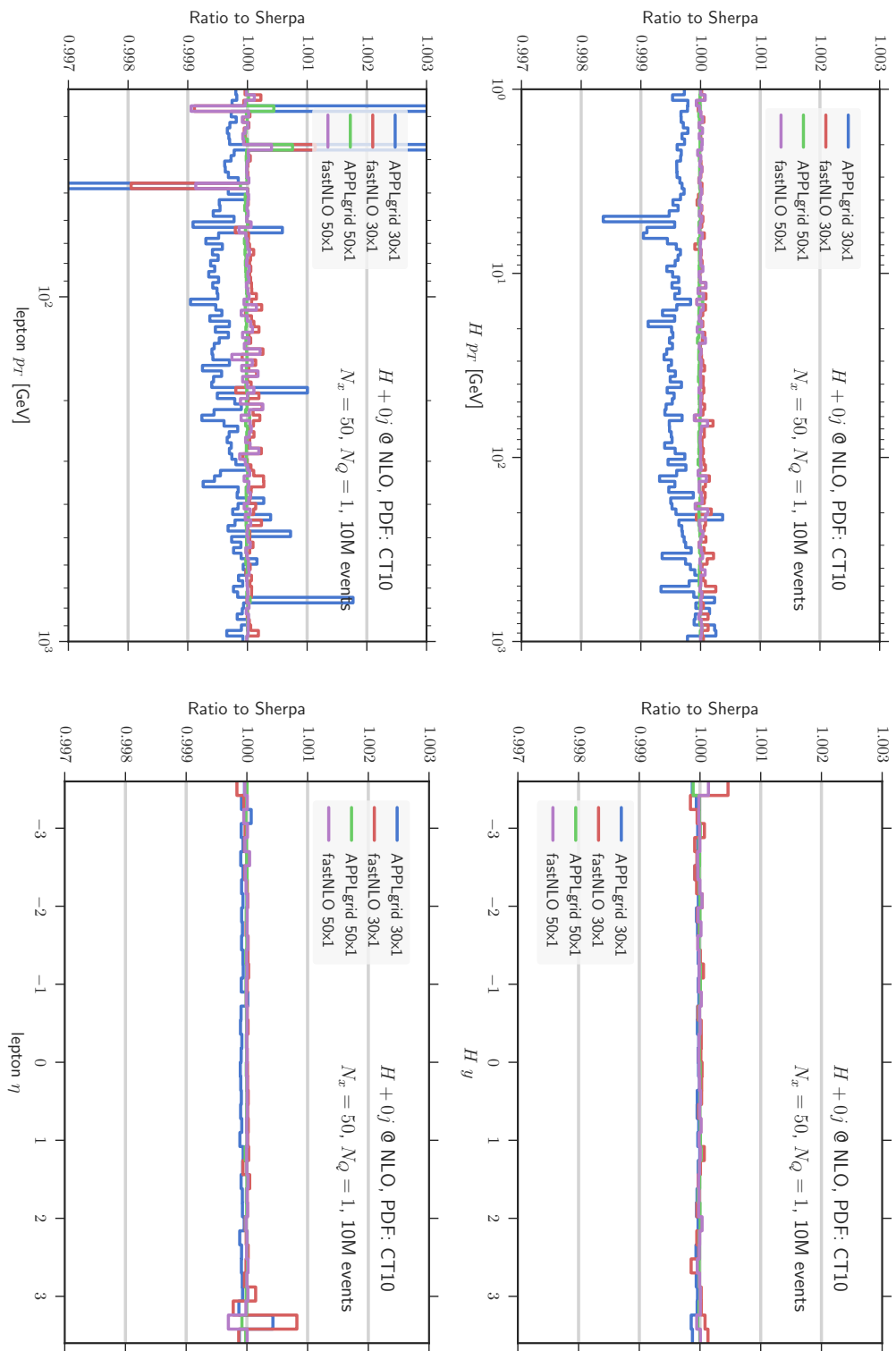
In this section we will prove, that the grids are able to reproduce the reference distributions up to the available interpolation accuracy. For each observable, one high precision grid and one lower precision grid is used. In the 0- and 1-jet cases, the high precision grid has 50 bins in  $x$  and the lower precision grid has 30 bins in  $x$ . In the 2-jet case, the high precision grid has 70 bins and the lower precision one has 50 bins. This is because with higher jet multiplicity, the influence of high  $x$  values increases while in all cases the same transformation is used to smooth the distribution. As we have seen in [?????????????????????????????????](#), this transformation favors low values of  $x$ , so a relatively high number of grid points is needed to accurately represent the high  $x$  region. For all the following calculations, the scale parameters have been fixed to the mass of the Higgs boson. Therefore,  $Q^2$  does not change and

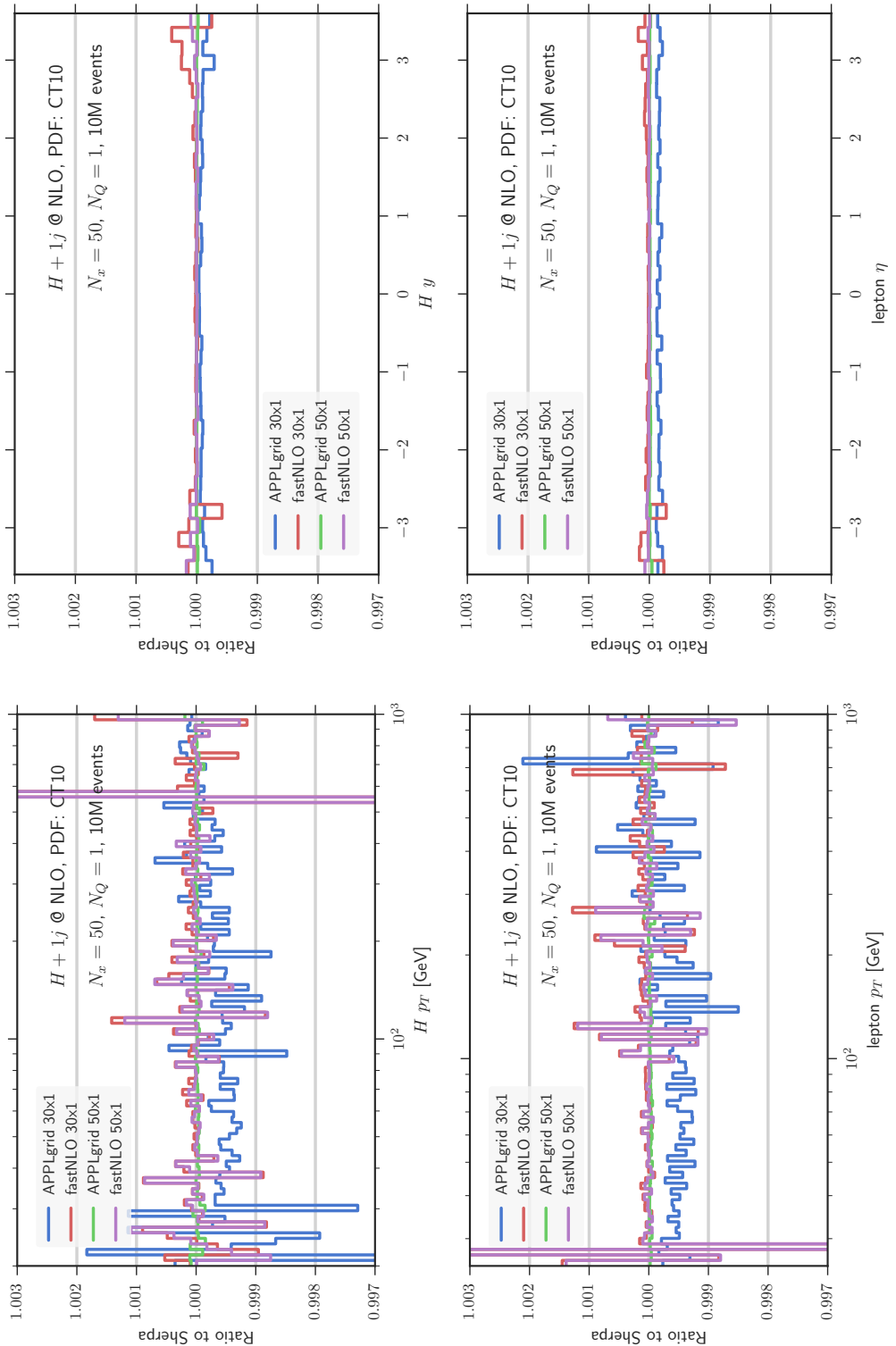
only one bin is used. To achieve better comparability, **APPLGRID** is configured to use fourth order interpolation, which is the same as is hardcoded into the **fastNLO** library. A sample of 1 million events is used to fill the grids.

Figure 4.4 shows the ratio of the results obtained by convoluting the grids with the CT10 PDF to the reference distributions for the 0-jet process. Using the high precision grid, almost all bins show errors below 0.1 %. **APPLGRID** and **fastNLO** show roughly the same accuracy but the lepton  $p_{\perp}$  shows a few outliers with **fastNLO**. The effect of using a smaller grid is considerably bigger for the  $p_{\perp}$  distributions than for the rapidity distributions. It is also bigger for **APPLGRID** than for **fastNLO**.

With one jet (fig. 4.5), the errors in the reproduction of the  $p_{\perp}$  become notably larger, especially when using **fastNLO**. There are comparatively large outliers using the lower precision grids. Nonetheless, with the high precision grids the errors are still within 0.3 %.

The case of two jets is shown in fig. 4.6. Here the grid with 50 bins produces relatively large errors. Though the plot does not comprise this, the highest errors are at the order of one percent. However ...

**Figure 4.4:** H+0j NLO

**Figure 4.5:** H+1j NLO

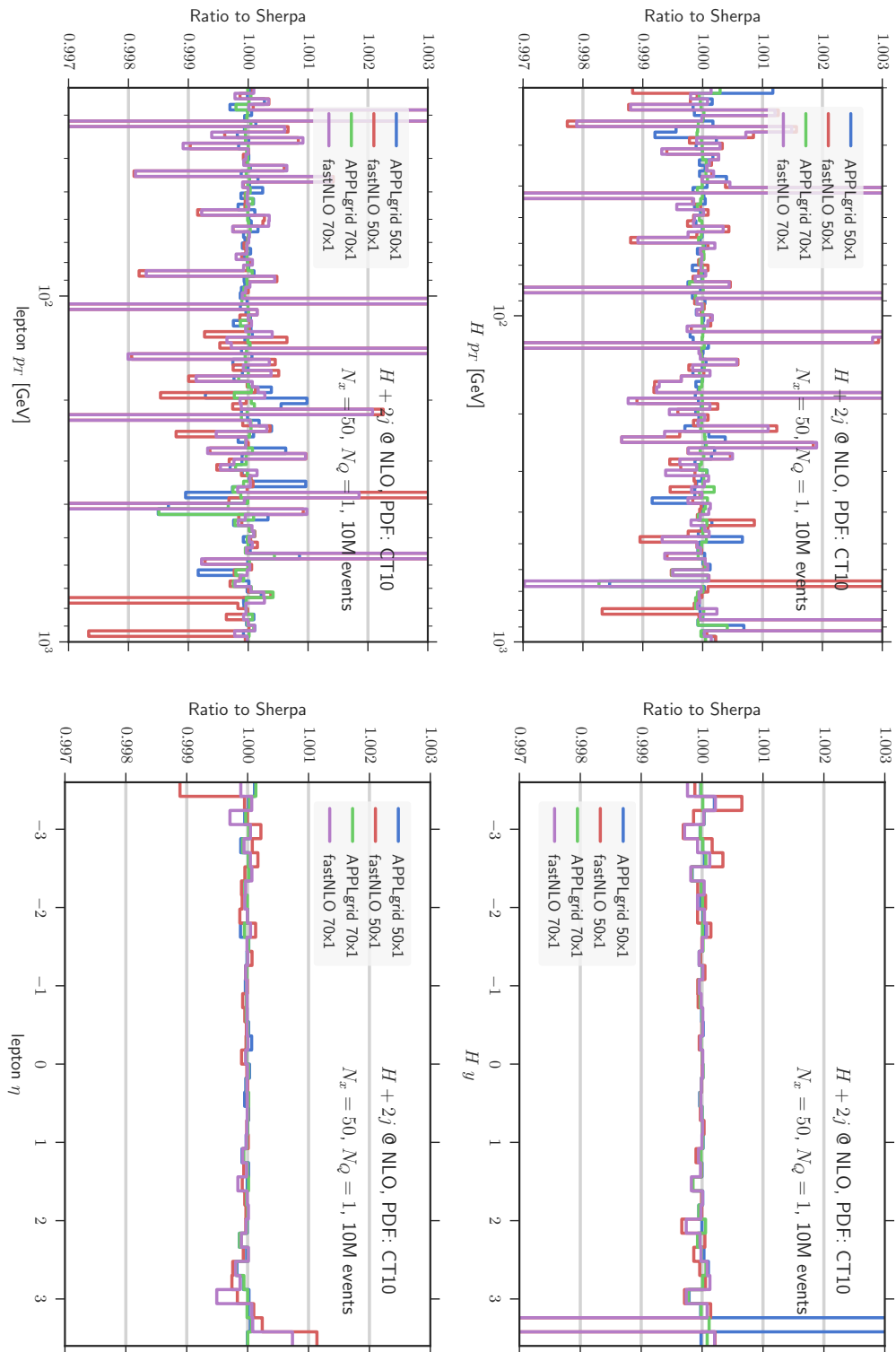


**Figure 4.6:**  $H+2j$  NLO

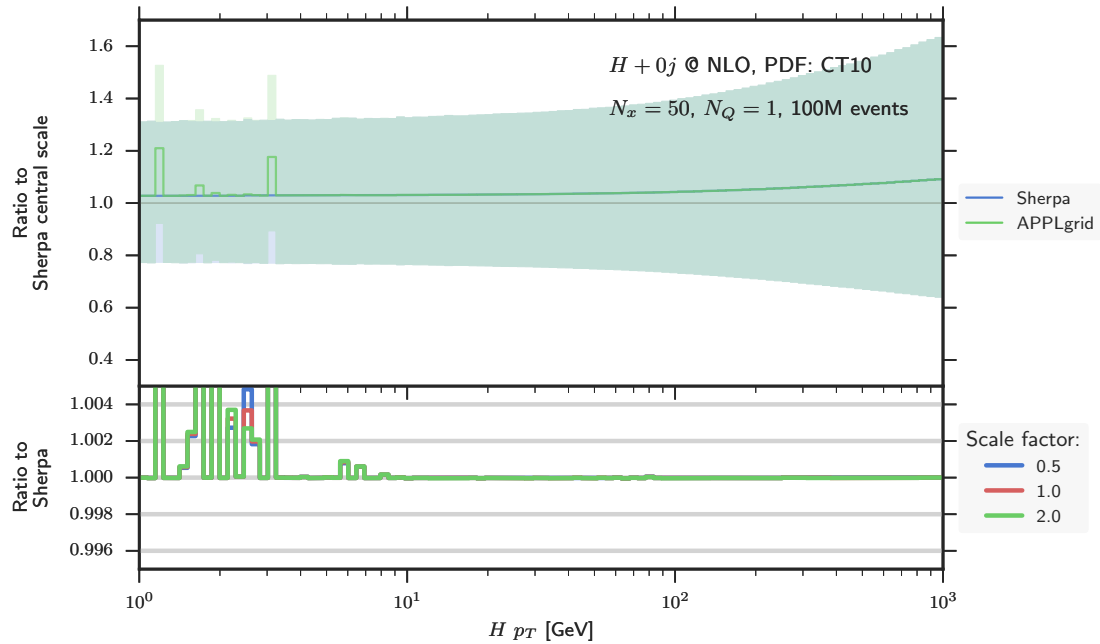


**Figure 4.7:** Scale variation appl

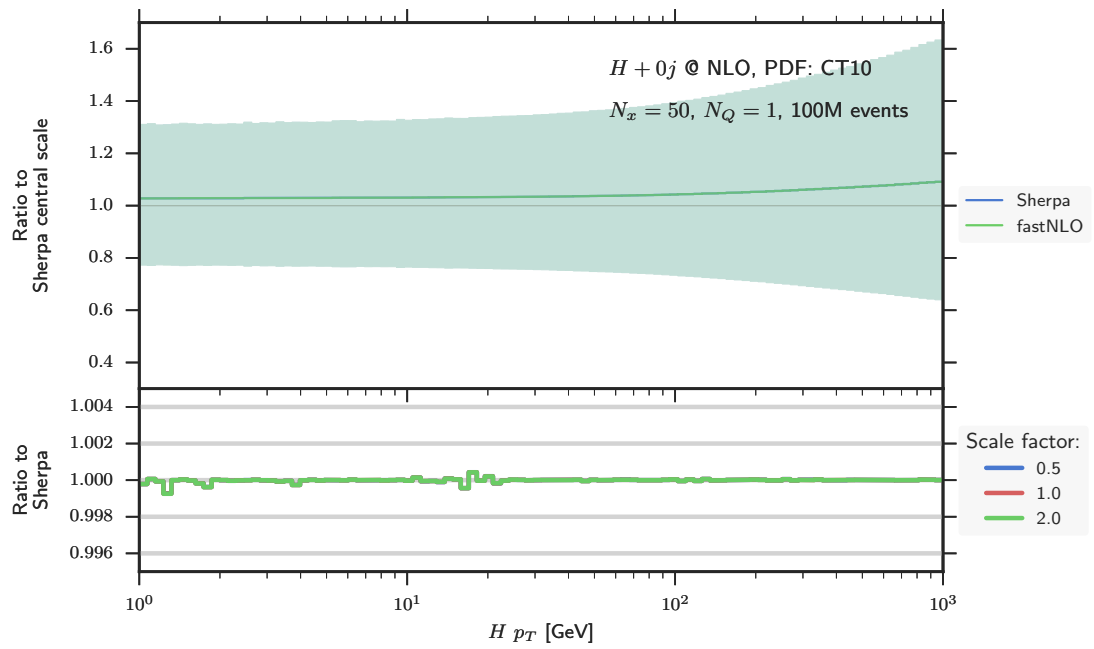


**Figure 4.8:** Scale variation fnlo

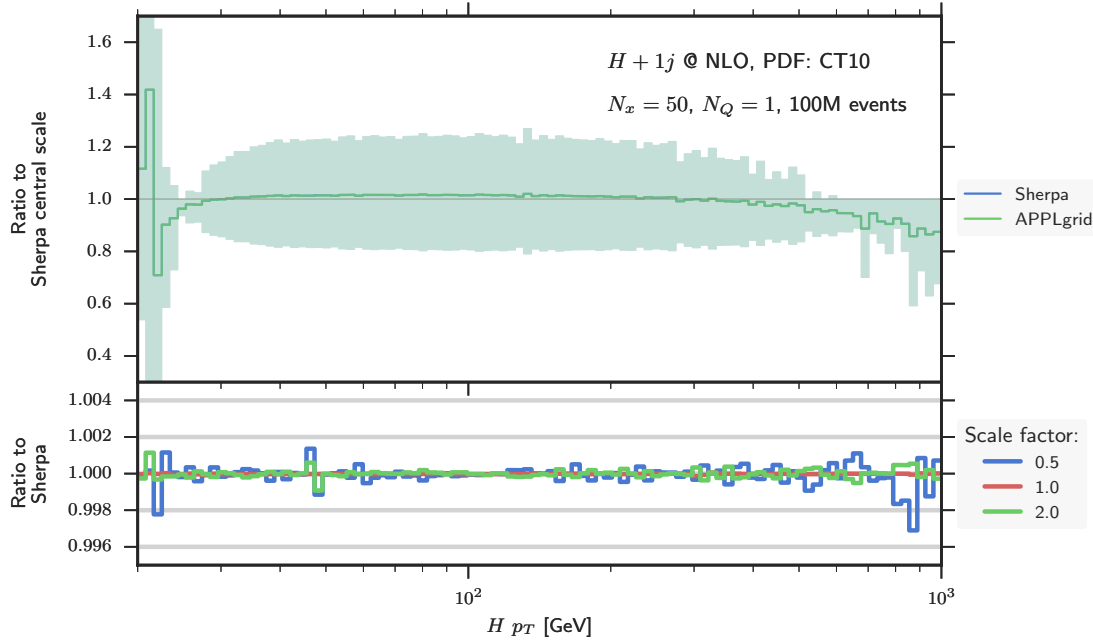


**Figure 4.9:** Scale variation appl

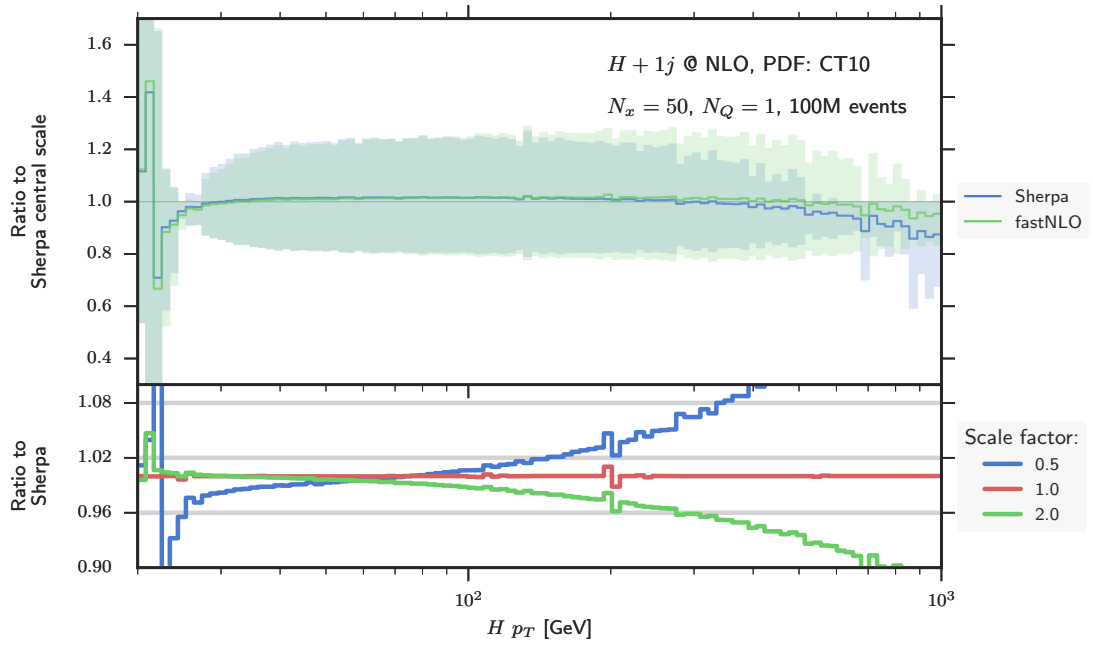


**Figure 4.10:** Scale variation fnlo

### 4.3 Application example: PDF uncertainty in cross section calculations

The application of the interpolation method is sensible every time a calculation has to be repeated plenty of times. This situation is given, when the uncertainty from a PDF set is meant to be included in a cross section calculation. Modern PDF sets contain a large number of different samples that can be used to derive the inherent uncertainty. Here we consider the NNPDF 3.0 NLO set [45], which consists of 101 samples each for 5 different values of  $\alpha_s$  between 0.115 and 0.121. The grid that has been filled with 100 million events using the central value of the CT10 set is used to calculate a total of 505 replicas for the Higgs  $p_\perp$  in fig. 4.11.

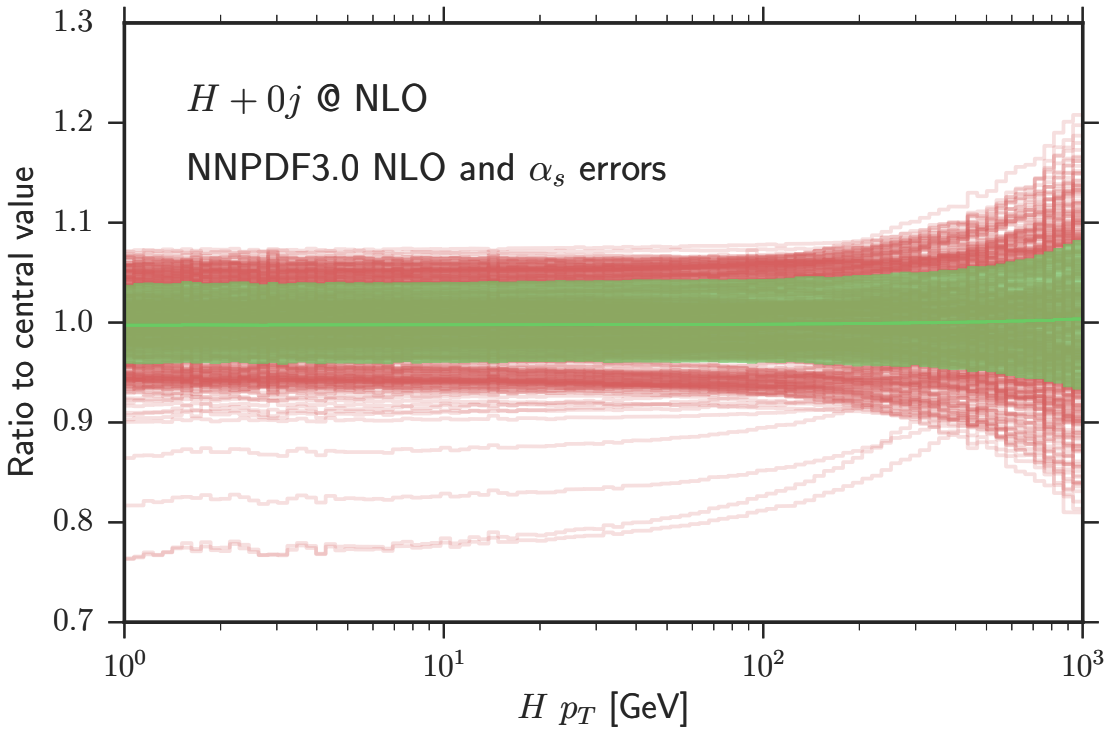


**Figure 4.11:** Application example of the interpolation method. The figure shows the distribution of replicas from the NNPDF3.0 NLO set including the error on  $\alpha_s$  for the  $p_\perp$  of the Higgs boson in gluon fusion. The green area highlights the  $1-\sigma$  confidence interval.

#### 4.4 Application example: Detailed scale dependence of the cross section

When one wishes to estimate the uncertainty of a fixed order calculation, a common method is to vary the renormalization and factorization scales simultaneously or independently by some factor, usually a factor of 2. This way one hopes to get a reasonable estimate of the corrections due to higher order terms. Typically, only the boundary values are calculated because of limited resources. However, using interpolation grids, any combination of scale factors can be evaluated very fast. To demonstrate this, fig. 4.12 shows the total cross section of inclusive Higgs production through gluon fusion for different combinations of scale factors, calculated using a `fastNLO` grid. Both the renormalization scale and the factorization scale are independently varied by 13 factors between  $\frac{1}{4}$  and 4 resulting in a total number of

169 calculations of the cross section.

We see that the dependence on the factorization scale is low whereas we observe a strong dependence on the renormalization scale.

Calculations such as this one and the example illustrated before would be extremely costly if done explicitly. If they are time-critical, explicit calculations become impossible. Interpolation tools offer much more flexibility in these cases.

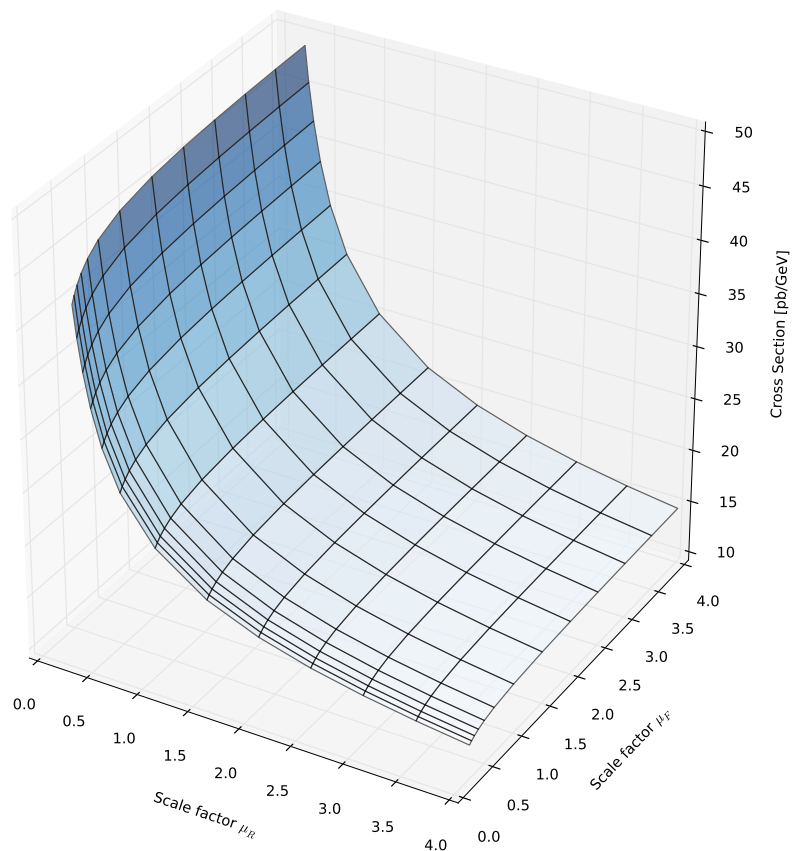


**Figure 4.12:** Application example of the interpolation method

# CHAPTER 5

---

## Diskussion

---



# CHAPTER 6

---

## Conclusion

---

...

Version 2.0 of `MCgrid` will allow the creation of grids for calculations matching NLO QCD computations and parton showers using `MC@NLO`. This has not been verified yet for Higgs production. However, as has been seen in section [???](#) the `MC@NLO` approach allows for a more accurate description of soft and collinear emissions than fixed order NLO calculations. Therefore ...

In section [???](#) we examined, how `APPLGRID` and `fastNLO` parametrize the  $x$ -distribution to provide a better coverage of the data on a grid with equal-sized bins. Which transformation should be used depends on the considered observable. To achieve the best possible performance, one would have to check the actual  $x$ -distribution in each case. The provided transformations are obviously a compromise to cover the needs of a large number of processes. The drawback of this approach is, that for some observables one needs unnecessary large grids to reliably reproduce them. There is, however, an alternative way: When performing the phasespace run prior to the fill run, one could, instead of only determining the limit values of  $x$  and  $Q^2$ , sample the whole distribution. By the use of numerical inversion, the data could then be used to provide a transformation that represents the actual distribution of  $x$  or  $Q^2$  in the process. Thus, the bins of the grid would be filled ideally and a smaller grid would suffice to reproduce the desired observable. This would improve the overall performance of the software, as a smaller grid means less computation time and less memory consumption.



---

## List of Figures

---

2.1	UV-divergent loop diagram . . . . .	4
2.2	Feynman diagrams for gluon emission in $e^+e^-$ annihilation . . . . .	6
2.3	Virtual correction in $e^+e^-$ annihilation . . . . .	7
2.4	Feynman diagrams for initial-state gluon emission . . . . .	8
2.5	Example of a parton shower. . . . .	10
2.6	Higgs production through gluon fusion. . . . .	18
2.7	Example diagrams illustrating the QCD corrections to the process $pp \rightarrow H$ : (a), (b) virtual corrections; (c), (d) real emission of a gluon; (e) $gq \rightarrow Hq$ ; (f) $q\bar{q} \rightarrow Hg$ . . . . .	20
2.8	Effective Higgs coupling. . . . .	21
2.9	Higgs decay into two $\tau$ leptons. . . . .	22
3.1	The transformations applied to the $x$ distribution, normalized to the range $[0, 1]$ . . . . .	24
3.2	The event fraction per bin for the different transformations. . . . .	25
3.3	The transverse momentum $p_\perp$ of the Higgs boson differential in the momentum fraction $x$ of one of the gluons. . . . .	26
3.4	The rapidity $y$ of the Higgs boson differential in the momentum fraction $x$ of one of the gluons. . . . .	26
4.1	$H$ pT 0j . . . . .	28
4.2	$H$ pT 1j . . . . .	29
4.3	$H$ pT 2j . . . . .	29
4.4	$H+0j$ NLO . . . . .	32

4.5	H+1j NLO . . . . .	33
4.6	H+2j NLO . . . . .	34
4.7	Scale variation appl . . . . .	35
4.8	Scale variation fnlo . . . . .	35
4.9	Scale variation appl . . . . .	36
4.10	Scale variation fnlo . . . . .	36
4.11	Application example of the interpolation method. The figure shows the distribution of replicas from the NNPDF3.0 NLO set including the error on $\alpha_s$ for the $p_\perp$ of the Higgs boson in gluon fusion. The green area highlights the $1-\sigma$ confidence interval. . . . .	38
4.12	Application example of the interpolation method . . . . .	40

---

## List of Tables

---



---

## Listings

---



---

## Bibliography

---

- [1] R. P. Feynman, Phys. Rev. Lett. **23**, 1415 (1969).
- [2] G. Sterman et al., Rev. Mod. Phys. **67**, www.phys.psu.edu/ cteq/handbook/v1.1/handbook.pdf, 157 (1995).
- [3] G. P. Salam, (2010), arXiv:1011.5131 [hep-ph].
- [4] R. K. Ellis, W. J. Stirling, and B. R. Webber, *QCD and Collider Physics*, Cambridge monographs on particle physics, nuclear physics, and cosmology (Cambridge Univ. Press, Cambridge, 1996).
- [5] S. Moch, J. Vermaseren, and A. Vogt, Nucl.Phys. **B688**, 101 (2004), arXiv:hep-ph/0403192 [hep-ph].
- [6] A. Vogt, S. Moch, and J. Vermaseren, Nucl.Phys. **B691**, 129 (2004), arXiv:hep-ph/0404111 [hep-ph].
- [7] Z. Kunszt and D. E. Soper, Phys. Rev. D **46**, 192 (1992).
- [8] S. Frixione and B. R. Webber, JHEP **0206**, 029 (2002), arXiv:hep-ph/0204244 [hep-ph].
- [9] S. Catani and M. Seymour, Nucl.Phys. **B485**, 291 (1997), arXiv:hep-ph/9605323 [hep-ph].
- [10] L. Del Debbio, N. P. Hartland, and S. Schumann, Comput.Phys.Commun. **185**, 2115 (2014), arXiv:1312.4460 [hep-ph].
- [11] T. Carli, D. Clements, A. Cooper-Sarkar, C. Gwenlan, G. P. Salam, et al., Eur.Phys.J. **C66**, 503 (2010), arXiv:0911.2985 [hep-ph].

- [12] T. Kluge, K. Rabbertz, and M. Wobisch, 483 (2006), arXiv:[hep-ph/0609285](#) [hep-ph].
- [13] M. Wobisch, D. Britzger, T. Kluge, K. Rabbertz, and F. Stober, (2011), arXiv:[1109.1310](#) [hep-ph].
- [14] P. Higgs, Physics Letters **12**, 132 (1964).
- [15] P. W. Higgs, Phys. Rev. Lett. **13**, 508 (1964).
- [16] F. Englert and R. Brout, Phys. Rev. Lett. **13**, 321 (1964).
- [17] G. S. Guralnik, C. R. Hagen, and T. W. B. Kibble, Phys. Rev. Lett. **13**, 585 (1964).
- [18] Y. Nambu, Phys. Rev. **117**, 648 (1960).
- [19] P. W. Anderson, Phys. Rev. **130**, 439 (1963).
- [20] G. Aad et al., Physics Letters B **716**, 1 (2012).
- [21] S. Chatrchyan et al., Physics Letters B **716**, 30 (2012).
- [22] S. Dittmaier et al., (2011) 10.5170/CERN-2011-002, arXiv:[1101.0593](#) [hep-ph].
- [23] H. M. Georgi, S. L. Glashow, M. E. Machacek, and D. V. Nanopoulos, Phys. Rev. Lett. **40**, 692 (1978).
- [24] D. Graudenz, M. Spira, and P. M. Zerwas, Phys. Rev. Lett. **70**, 1372 (1993).
- [25] A. Djouadi, M. Spira, and P. Zerwas, Physics Letters B **264**, 440 (1991).
- [26] A. Djouadi, Phys.Rept. **457**, 1 (2008), arXiv:[hep-ph/0503172](#) [hep-ph].
- [27] R. V. Harlander and W. B. Kilgore, Phys. Rev. Lett. **88**, 201801 (2002).
- [28] C. Anastasiou and K. Melnikov, Nucl.Phys. **B646**, 220 (2002), arXiv:[hep-ph/0207004](#) [hep-ph].
- [29] C. Anastasiou, K. Melnikov, and F. Petriello, Nucl.Phys. **B724**, 197 (2005), arXiv:[hep-ph/0501130](#) [hep-ph].
- [30] S. Catani and M. Grazzini, Phys.Rev.Lett. **98**, 222002 (2007), arXiv:[hep-ph/0703012](#) [hep-ph].

- [31] X. Chen, T. Gehrmann, E. Glover, and M. Jaquier, Phys.Lett. **B740**, 147 (2015), arXiv:1408.5325 [hep-ph].
- [32] D. de Florian, M. Grazzini, and Z. Kunszt, Phys.Rev.Lett. **82**, 5209 (1999), arXiv:hep-ph/9902483 [hep-ph].
- [33] V. Ravindran, J. Smith, and W. Van Neerven, Nucl.Phys. **B634**, 247 (2002), arXiv:hep-ph/0201114 [hep-ph].
- [34] J. M. Campbell, R. K. Ellis, and C. Williams, Phys.Rev. **D81**, 074023 (2010), arXiv:1001.4495 [hep-ph].
- [35] H. van Deurzen, N. Greiner, G. Luisoni, P. Mastrolia, E. Mirabella, et al., Phys.Lett. **B721**, 74 (2013), arXiv:1301.0493 [hep-ph].
- [36] G. Cullen, H. van Deurzen, N. Greiner, G. Luisoni, P. Mastrolia, et al., Phys.Rev.Lett. **111**, 131801 (2013), arXiv:1307.4737 [hep-ph].
- [37] S. Dittmaier, S. Dittmaier, C. Mariotti, G. Passarino, R. Tanaka, et al., (2012) 10.5170/CERN-2012-002, arXiv:1201.3084 [hep-ph].
- [38] S. Heinemeyer et al., edited by S. Heinemeyer (2013) 10.5170/CERN-2013-004, arXiv:1307.1347 [hep-ph].
- [39] G. Aad et al., JHEP **1504**, 117 (2015), arXiv:1501.04943 [hep-ex].
- [40] S. Chatrchyan et al., JHEP **1405**, 104 (2014), arXiv:1401.5041 [hep-ex].
- [41] J. M. Campbell, R. K. Ellis, and G. Zanderighi, JHEP **10**, 028 (2006), arXiv:hep-ph/0608194 [hep-ph].
- [42] M. Cacciari, G. P. Salam, and G. Soyez, Eur.Phys.J. **C72**, 1896 (2012), arXiv:1111.6097 [hep-ph].
- [43] M. Cacciari, G. P. Salam, and G. Soyez, JHEP **0804**, 063 (2008), arXiv:0802.1189 [hep-ph].
- [44] H.-L. Lai, M. Guzzi, J. Huston, Z. Li, P. M. Nadolsky, et al., Phys.Rev. **D82**, 074024 (2010), arXiv:1007.2241 [hep-ph].
- [45] R. D. Ball et al., JHEP **04**, 040 (2015), arXiv:1410.8849 [hep-ph].



---

## Danksagung

---



**Erklärung** nach §13(8) der Prüfungsordnung für den Bachelor-Studiengang Physik und den Master-Studiengang Physik an der Universität Göttingen:

Hiermit erkläre ich, dass ich diese Abschlussarbeit selbstständig verfasst habe, keine anderen als die angegebenen Quellen und Hilfsmittel benutzt habe und alle Stellen, die wörtlich oder sinngemäß aus veröffentlichten Schriften entnommen wurden, als solche kenntlich gemacht habe.

Darüberhinaus erkläre ich, dass diese Abschlussarbeit nicht, auch nicht auszugsweise, im Rahmen einer nichtbestandenen Prüfung an dieser oder einer anderen Hochschule eingereicht wurde.

Göttingen, den July 24, 2015

(Timo Janßen)



---

## **Todo list**

---